AGU PUBLICATIONS

JGR

Journal of Geophysical Research: Atmospheres

RESEARCH ARTICLE
10.1002/2015JD024591

Key Points:
- The compression effect of the Tibetan Plateau on cloud vertical structure
- The longwave CRE in the atmosphere over the Tibetan Plateau is a net cooling effect
- Unique vertical structure of CRE over the Tibetan Plateau

Correspondence to:
Y. Liu and J. Lu,
lym@lasg.iap.ac.cn;
jlu4@fsu.edu

Citation:
Yan, Y., Y. Liu, and J. Lu (2016), Cloud vertical structure, precipitation, and cloud radiative effects over Tibetan Plateau and its neighboring regions, *J. Geophys. Res. Atmos.*, *121*, 5864–5877, doi:10.1002/2015JD024591.

Received 2 DEC 2015
Accepted 2 MAY 2016
Accepted article online 5 MAY 2016
Published online 21 MAY 2016

Cloud vertical structure, precipitation, and cloud radiative effects over Tibetan Plateau and its neighboring regions

Yafei Yan[1,2], Yimin Liu[1], and Jianhua Lu[1,3]

[1]State Key Laboratory of Numerical Modeling for Atmospheric Sciences and Geophysical Fluid Dynamics, Institute of Atmospheric Physics, Chinese Academy of Sciences, Beijing, China, [2]College of Earth Science, University of Chinese Academy of Sciences, Beijing, China, [3]Center for Ocean-Atmospheric Prediction Studies, Florida State University, Tallahassee, Florida, USA

Abstract The vertical structure of clouds and its connection with precipitation and cloud radiative effects (CRE) over the Tibetan Plateau (TP) are analyzed and compared with its neighboring land and tropical oceans based on CloudSat and Cloud-Aerosol Lidar and Infrared Pathfinder Satellite Observations (CALIPSO) products and the Tropical Rainfall Measuring Mission (TRMM) precipitation data. Unique characteristics of cloud vertical structure and CRE over the TP are found. The cloud amount shows seasonal variation over the TP, which presents a single peak (located in 7–11 km) during January to April and two peaks (located in 5–8 km and 11–17 km separately) after mid-June, and then resumes to one peak (located in 5–10 km) after mid-August. Topography-induced restriction on moisture supply leads to a compression effect on clouds, i.e., the reduction in both cloud thickness and number of cloud layers, over the TP. The topography-induced compression effect is also shown in the range in the variation of cloud thickness and cloud-top height corresponding to different precipitation intensity, which is much smaller over the TP than its neighboring regions. The longwave CRE in the atmosphere over the TP is a net cooling effect. The vertical structure of CRE over the TP is unique compared to other regions: there exists a strong cooling layer of net CRE at the altitude of 8 km, from June to the beginning of October; the net radiative heating layer above the surface is shallower but stronger underneath 7 km and with a stronger seasonal variation over the TP.

1. Introduction

Cloud plays an important role in the energy cycle and balance of the Earth's climate system by influencing the radiative effects and also the latent heating or cooling caused by the phase changes of water in the clouds [*Ramanathan et al.*, 1989; *Rossow and Lacis*, 1990; *Wielicki et al.*, 1995; *Li et al.*, 1995; *Stephens*, 2005; *Yang et al.*, 2010; *Huang*, 2013]. The Tibetan Plateau (TP) significantly affects the atmospheric circulation and Asian climate [*Wu and Zhang*, 1998; *Duan and Wu*, 2005; *Liu et al.*, 2007a, 2007b; *Duan et al.*, 2008]. However, the detailed knowledge about cloud and its role in general circulation and climate over the TP is still unclear due to the very sparse observation before the 1970s. Since then, this situation has been improved with the appearance of satellite remote-sensing observation. Previous researchers have studied the cloud characteristics over the TP by using various satellite data [*Su and Mao*, 1998; *Gao et al.*, 2003; *Li et al.*, 2004; *Yu et al.*, 2004; *Chen and Liu*, 2005; *Li et al.*, 2006]. However the earlier satellite data, such as from ISCCP (the International Satellite Cloud Climatology Project) and MODIS (the Moderate Resolution Imaging Spectroradiometer), do exist limitations. For example, the thin clouds are indistinguishable from aerosols in ISCCP when optical thickness is less than 0.3–0.5 [*Rossow and Garder*, 1993]; Both ISCCP and MODIS underestimate low-level clouds and overestimate middle-level cloud comparing to the station-based observation over the TP [*Li et al.*, 2006; *Naud and Chen*, 2010]. The precipitation radar and TRMM Microwave Imager onboard the Tropical Rainfall Measuring Mission (TRMM) satellite are helpless in observing small-size particles despite of its capability of penetrating rainy cloud and obtaining the internal three-dimensional information, and only larger rainfall particles can be observed due to limitations of its working broadband. Hence, conventional passive-sensor satellite data, largely missing the comprehensive information on the vertical distribution of cloud layers, can only crudely estimate the location and vertical extent of clouds [*Cooperative Institute for Research in the Atmosphere*, 2008]. On the other hand, current climate models still cannot accurately simulate the vertical structure of clouds (Figure 1), reflecting the

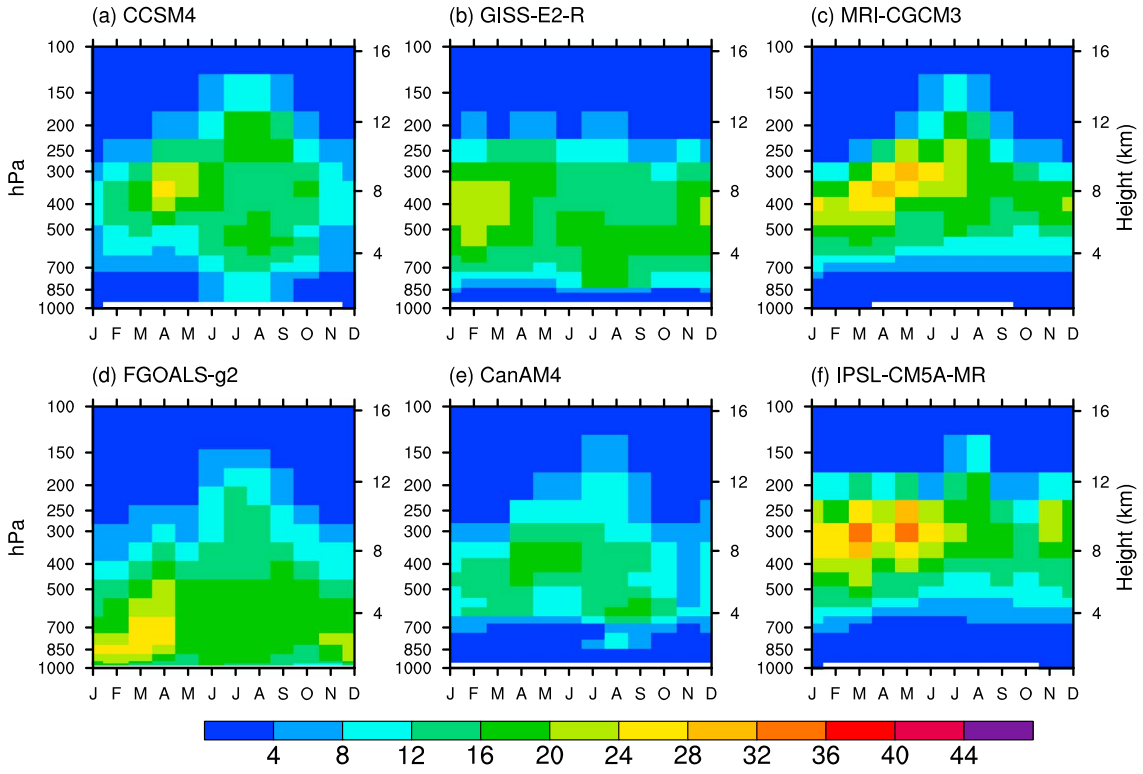

Figure 1. Monthly cloud amount over the TP (27°N–40°N, 70°E–103°E, altitude: >3000 m) simulated by different climate models. Unit: %.

shortcoming of the models in simulating cloud-related physical processes [*Zhang et al*., 2005; *Dufresne and Bony*, 2008; *Jiang et al*., 2012; *Lu et al*., 2014].

In April 2006, NASA (National Aeronautics and Space Administration) launched CloudSat satellite [*Stephens et al*., 2002] carrying cloud profile radar (CPR; hereafter referred as radar) and CALIPSO satellite [*Winker et al*., 2007] carrying Cloud-Aerosol Lidar with Orthogonal Polarization (CALIOP; hereafter referred as lidar) in California, which are designed to fly in nearly identical orbits and successfully joined the "A-Train" constellation. On one hand, the CPR is a 94 GHz nadir-looking radar which is able to penetrate the optically thick clouds, on the other hand, while CALIOP is able to detect tenuous cloud layer that are below the detection threshold of radar. In other words, it has the ability to detect shallow clouds. Therefore, accurate location of cloud top and complete vertical structure information of cloud can be obtained by the combined use of CPR and CALIOP, because of their unique complementary skills. Previous researches have shown that CloudSat/CALIPSO data are credible compared with ISCCP and ground observation data [*Sassen and Wang*, 2008; *Wang et al*., 2010a; *Naud and Chen*, 2010; *Kim et al*., 2011; *Noh et al*., 2011; *Jiang et al*., 2011].

Although the clouds over the TP have attracted wide attention [*Wang et al*., 2010a, 2010b, 2011; *Luo et al*., 2011; *Rüthrich et al*., 2013; *Peng et al*., 2014; *Zhang et al*., 2014; *Hong and Liu*, 2015], the vertical structure of clouds and their radiative effects remain unclear and deserve further research. Of particular interest is the interaction between precipitation, the clouds including their vertical structure, and atmospheric circulation, for which the observations from CloudSat/CALIPSO may provide useful information and clues. In this article we intend to investigate the features of clouds and precipitation observed from CloudSat/CALIPSO over the TP by the comparison with its neighboring land regions and tropical ocean regions in the south of the TP. The definition of the three areas are as follows: TP (27°N–40°N, 70°E–103°E, altitude: >3000 m); NIST (20°N–27°N, 70°E–103°E); TO (20°S–20°N, 60°E–150°E, over ocean only), as shown in Figure 2. Except for their neighboring with the TP, the other two regions are chosen because they represent the regions of deep convections during the summer time over the land and the ocean, respectively, as well as there are little spatial and dynamic heterogeneity involved in each region.

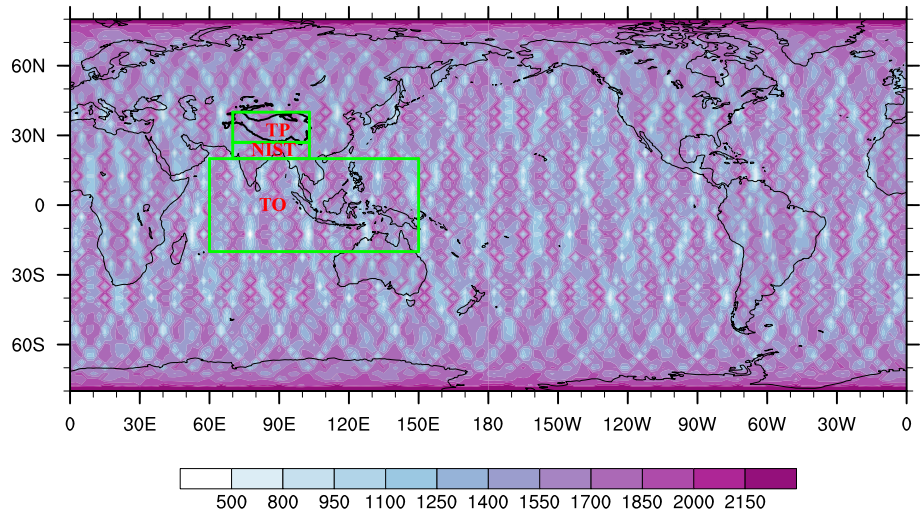

Figure 2. The global distribution of the total number of valid samples during January 2007 of the CloudSat/CALIPSO data in 2.5° × 2.5° grid cells, and the geographical location of the TP, NIST, and TO regions for this study. The bold curve in the TP box represents where the altitude is 3000 m.

The paper is organized as follows. Section 2 is the data and methodology. Section 3 presents the results about the vertical structure of clouds and its relationship with precipitation, and also the vertical structure of cloud radiative effects. Section 4 is the conclusions and discussion.

2. Data and Methodology

The data period of CloudSat/CALIPSO products is between June 2006 and April 2011 (Table 1). The periods when the CPR failed to work have been excluded in the diagnostics. 2B-GEOPROF-LIDAR data set is obtained by combining the information from sensors of CPR and CALIOP, and it can divide the vertical profile into clear sky or 1–5 layers of clouds according to the existence of cloud, and meanwhile provides each cloud layer's top height and base height [*Jet Propulsion Laboratory* (*JPL*), 2007]. 2B-GEOPROF-LIDAR product also provides cloud amount, which is defined as the fraction of lidar volumes in a radar resolution volume that contains hydrometeors [*Mace et al*., 2012]. 2B-FLXHR-LIDAR data set provides upwelling and downwelling longwave and shortwave fluxes at discrete levels of atmospheric profiles, and then the corresponding heating rates are inferred from these fluxes. The computation makes use of liquid and ice water content estimated from the CPR, and additional clouds and aerosol properties detected by CALIPSO and MODIS, combining with the auxiliary information from the ECMWF reanalysis atmospheric state [*JPL*, 2011]. Note that, according to *JPL* document (2011), the pixels with flag values of eight or less should contain valid flux and heating rate output, and this is the criterion of valid data adopted in the diagnostics.

In this study, we first calculate the product from original orbital data to daily data on grid points with the horizontal resolution being 2.5° × 2.5° and the vertical resolution being 240 m, wherein the cloud properties for each lattice is the average of all pixels passing through the grid box, so that there is only one value for each grid representing the average properties within meridional or zonal distance of 1.25°. The average number of valid samples for each grid cell in 1 month is about 1400 granules, and the global sample distribution is basically uniform, as shown in Figure 2. Note, however, that the statistics for the regional averages of the sole

Table 1. CloudSat/CALIPSO Products

CloudSat/CALIPSO Products	Variables	Time period
2B-GEOPROF-LIDAR.r04	Cloud fraction; number of cloud layers; top-, bottom- height of each cloud layer	15 Jun 2006 to 17 Apr 2011
2B-FLXHR-LIDAR.p2_r04	Top-of-atmosphere cloud radiative effect; bottom-of-atmosphere cloud radiative effect; heating rate; pixel status flag	6 Jul 2006 to 17 Apr 2011

cloud properties from CloudSat/CALIPSO are independent of the grid size, though we still use 2.5° × 2.5° gridded data in the calculation for cloud properties and cloud radiative effects.

We also used the same period of 3-hourly precipitation data from TRMM 3B42 (Version 6, whose horizontal resolution is 0.25° × 0.25°, [*Huffman et al.*, 2007]) together with the 2B-GEOPROF-LIDAR data set when calculating the relationship between the cloud vertical structure and precipitation. In addition, specific humidity and wind field data from ERA-Interim [*Simmons et al.*, 2006] in January from 2007 to 2011 and July from 2006 to 2010 are also used in order to explore the large-scale background of the seasonal difference in cloud amount over the TP and NIST.

In contrast to the sole regional average of cloud properties, the sorting between CloudSat/CALIPSO and TRMM data relies on the match of temporal-spatial scales, and hence we use the original CloudSat/CALIPSO profiles and available finest TRMM data (0.25° × 0.25° for each 3 h) to perform the sorting.

Based on the CloudSat/CALIPSO and TRMM data, we calculated the joint probability density function (PDF) of rainfall intensity and total cloud thickness (with the clear-sky thickness between adjacent cloud layers deducted) and the height of cloud top. Because the TRMM data and CloudSat/CALIPSO data are independent and are from different satellites, the temporal-spatial matching between them is necessary. The matching approach is as follows: (1) The original orbital CloudSat/CALIPSO profiles without spatial averaging are used; (2) for each CloudSat/CALIPSO profile, we seek the matching TRMM 3B42 precipitation on the 0.25° × 0.25° grid point that the position of cloud profile is located in, and the cloud and precipitation is near synchronous with the time difference being less than 1.5 h. The PDFs are only calculated over the ensemble of cloud-precipitation pairs with both observations being available. The binning of precipitation rate is based on the ranges (0–0.0001 mm/h, 0.0001–0.001 mm/h, 0.001–0.01 mm/h, 0.01–0.1 mm/h, 0.1–1 mm/h, 1–10 mm/h, and >10 mm/h), and the binning of the total cloud thickness is based on an equal 1 km interval, and 20 bins from 1 km to 20 km are used.

The cloud radiative effect (CRE), previously referred to as cloud radiative forcing (CRF) [*Ramanathan et al.*, 1989], is defined as the difference between radiation flux under all-sky and that under clear-sky conditions. Similarly, in this paper we calculate the CRE as the difference between radiation averaging over all-sky profiles and that averaging over clear-sky profiles. The CREs may be the cloud-induced net radiative influx for the total atmosphere-surface column (the CRE at the top of the atmosphere (TOA)), for the land or ocean columns (the CRE at the surface or the bottom of the atmosphere (BOA)), and for the total or part of atmospheric layer (the atmospheric CRE). Note that the atmospheric CRE per unit mass (in $W/m^2/100$ hPa) is equivalent to the cloud radiative heating (CRH, in K/d), and it is easy to obtain that 1 $W/m^2/100$ hPa of atmospheric CRE corresponds to about 0.085 K/d of CRH. Therefore, we directly use the available CRH to represent the atmospheric CRE, and we have checked with the atmospheric CRE obtained from the vertical profile of radiative fluxes and found that they are consistent with each other.

Note that because the CloudSat/CALIPSO observations are the subsample of the full diurnal cycles, there may exist substantial differences in the monthly or seasonal climatology of cloud and precipitation in this research when compared to the daily average climatology, especially over land [*Liu et al.*, 2008]. Therefore, we stress here that caveat and cautions should be taken in applying the results in the sense of climatology.

3. Results

3.1. Cloud Amount and Circulation Characteristics

The seasonal variation of the pentad-averaged cloud amount over the TP is the most obvious among the three regions, as shown in Figure 3. The cloud amount over the TP has a large value between 7 and 11 km from January to April, and the largest value (more than 44%, 9–10 km) occurs in the last pentad of March. During this period, the cloud amount has only one peak vertically [*Wang et al.*, 2011]. Since mid-May, the large value signal moves to lower altitudes (5–8 km). Meanwhile, the cloud amount (8%–20%) among 11–17 km increases, mainly due to the development of deep convections in eastern TP and leads to vertically double peaks in summer. After September, the cloud amount reverts to single peak (8–28%, 5–9 km).

The cloud amount over the NIST shows a dry-and-wet seasonal variation, and the clouds are mainly located in-between the high altitudes of 10–17.5 km. The cloud amount is always more than 44% during summer over the NIST, the largest of all the three regions. Over the TO, high clouds (12%–40%, 10–17.5 km) related

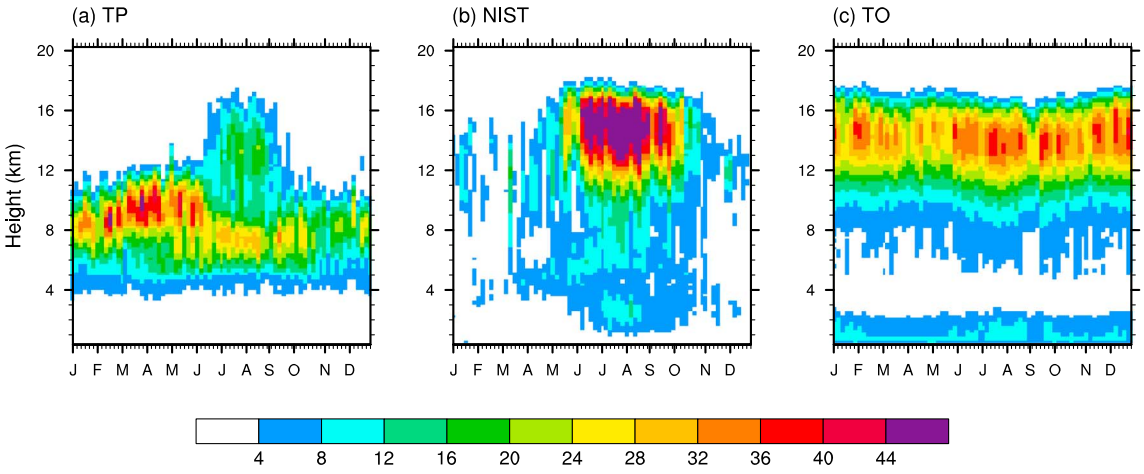

Figure 3. The pentad-averaged cloud amount over the (a) TP, (b) NIST, and (c) TO. Unit: %.

to deep convection appear all the year around. Because the TO region we defined in this study covers the Indo-Pacific warm pool with the seasonal march of SST, monsoons and Intertropical Convergence Zone included in the regional average, the deep convection and associated high clouds prevail throughout the year with little seasonal variation.

The difference between the seasonal variation of cloud amount over the TP and that of NIST may be partly explained from the large-scale circulation background and associated water vapor transport. A meridional cross section along 95°E is chosen to show the vertical profile of cloud amount and moisture transport because the maximum precipitation is nearby this longitude in summer monsoon [*Johansson et al.*, 2015].

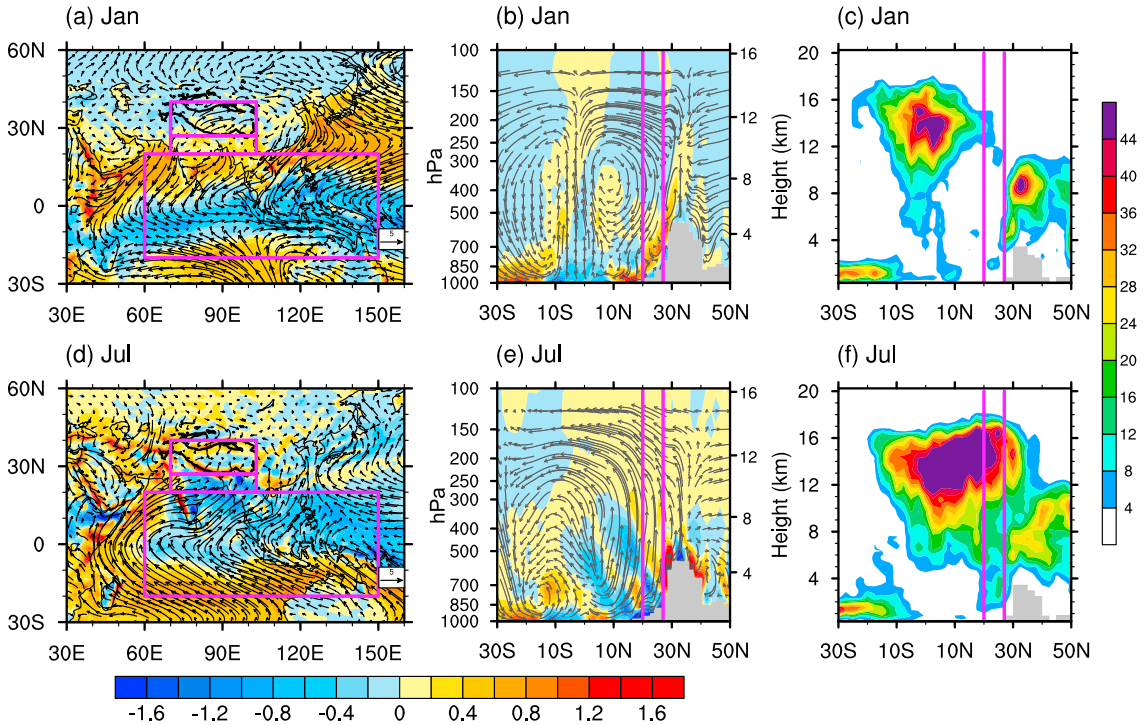

Figure 4. (a) 10 m wind (arrows, m/s) and the divergence of vertically integrated moisture flux (shadings, 10^{-4} kg s^{-1} m^{-2}) integrated from surface to 100 hPa; (b) the vertical profile of the divergence of moisture transport (shadings, 10^{-5} kg s^{-1} m^{-2}) and meridional-vertical velocity vectors (arrows) along 95°E; (c) the vertical profile of cloud amount (unit:%) along 95°E for January from 2007 to 2011. (d–f) The same as Figures 4a–4c but for July from 2006 to 2010.

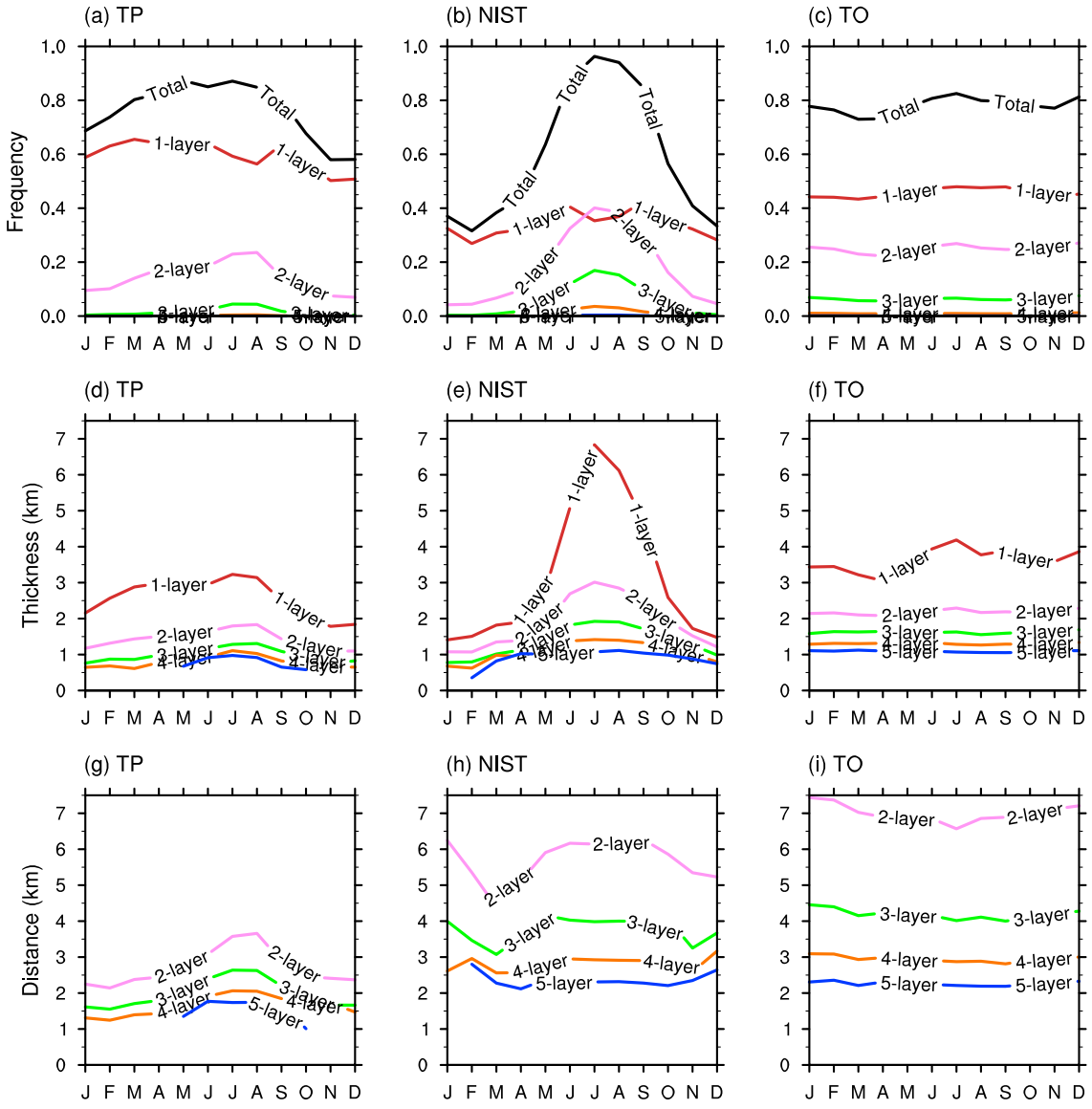

Figure 5. Monthly mean occurrence frequencies, relative to the times of all observations, of (a–c) total and one to five layer clouds, (d–f) average thickness of clouds, and (g–i) vertical distance between two adjacent cloud layers of multilayer clouds.

In winter, there is strong southwesterly wind bringing moist air at lower level over the TP (Figure 4a), and the upward motion below 10 km takes water vapor into high altitude (Figure 4b). The existence of downward velocity above 12 km makes the cloud concentrated below 12 km (Figure 4c). Over the NIST, the northerly wind near ground causes water vapor flux divergence, and the strong sinking motion are also disadvantageous for the formation of clouds (Figures 4a–4c). In summer, due to the outbreak of the Asian summer monsoon, abundant water vapor converges over the TP and NIST. Meanwhile, strong upward motion transport water vapor into higher altitudes, favoring the development of clouds (Figures 4d–4f). Previous researches [*Reiter and Gao*, 1982; *Luo and Yanai*, 1984; *Liu et al*., 2007a, 2007b; *Wu et al*., 2007] have shown that the TP plays a role of heating source in summer, and the radiative effect as well as the enhanced surface heating may enhance the convections over the TP. Hence, the more clouds above 12 km in summer over the TP are clearly related to the appearance of deep convection over the region. Compared to the deep convection over TP, the more abundant moisture supply and slope-induced upward motion favor a stronger deep convection over the NIST, and hence, the clouds there can reach nearly 18 km, higher than over the TP (Figure 4f).

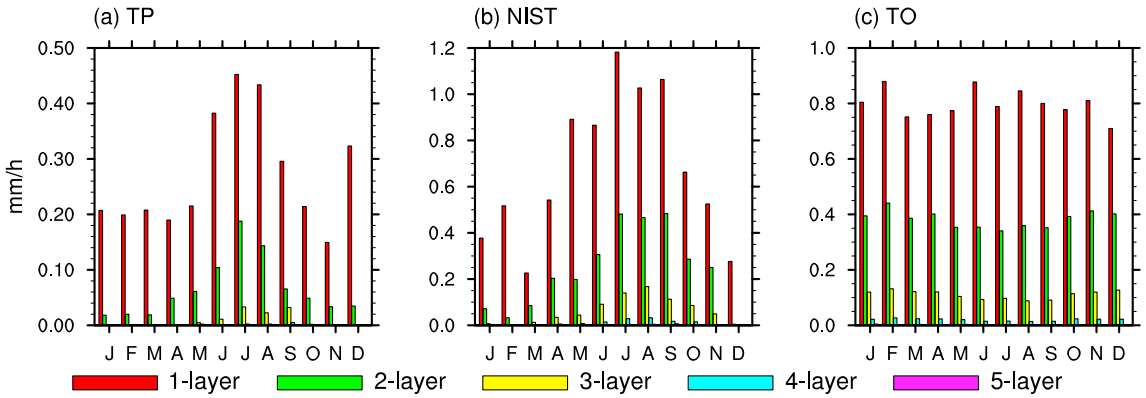

Figure 6. Monthly mean contribution of precipitation intensity corresponding to clouds of one to five layers to mean precipitation intensity over the (a) TP, (b) NIST, and (c) TO.

3.2. The Structure of Cloud Layers and Precipitation

Figure 5 shows the monthly frequencies of the occurrence, relative to the all available observations, of all clouds and clouds with one to five layers, of the average cloud thickness of each layer, and of the vertical distance between adjacent cloud layers. Consistent with the cloud amount, obvious seasonal variations in the occurrence frequencies of single-layer and multilayer clouds occur over the TP and NIST. While the multilayer clouds and also overall clouds occur more frequently in summer than in other seasons over the TP and NIST, the occurrence of single-layer clouds is more frequent than multilayer clouds during almost all of the months. Note the occurrence of multilayer clouds with the layer number larger than three is much less over the TP than over the NIST and TO. It is also found that both the averaged layer thickness and vertical distance between adjacent layers are the smallest over the TP than the other regions. These features suggest a compression effect of Tibetan Plateau terrain on the vertical layer structure of clouds. It is seen that the single-layer clouds over the NIST are thicker than those over the TO in summer, with the latter being comparable to the TP in thickness. This is because the single-layer clouds over the TO not only include the deep convective clouds but also have more cirrus clouds and also shallow convective clouds, while the single-layer clouds are mainly deep convective over the NIST.

Figure 6 illustrates the averaged contribution of precipitation intensity corresponding to clouds of one to five layers to mean precipitation intensity. It is seen that the single-layer clouds contribute most to the mean precipitation, while the multilayer clouds contribute much less to the averaged precipitation intensity. The intervals between multilayer clouds may suggest the discontinuity of liquid water in the vertical, not favorable to the occurrence of large precipitation. Multilayer clouds are likely to be accompanied by cloud dissipation, and hence, they may correspond to the decay phase of clouds and precipitation. Despite this similar feature over the three regions, we note that the precipitation rate over the TP is smaller than those over the other two regions, which is related to the lack of water supply over the plateau.

The joint probability distribution function (PDF) of total cloud thickness and precipitation intensity for the four seasons and annual mean conditions further illustrates the compression effect on the clouds and suppression effect on precipitation of the TP terrain (Figure 7). The range in the variation of total cloud thickness associated with a certain precipitation bin shows seasonal variations, especially over the TP. Take the rainfall bin of 0.1–1 mm/h as an example. In spring, the range in the variation of total cloud thickness is 0–9 km and the most likely range is 5–7 km; while it expands to 0–12 km and the most likely range relevant is 2–7 km during summer. Despite the seasonal differences, the largest PDFs of rainfall corresponding to thinner clouds, say less than 4 km, are mainly between the bins of 0.01–0.1 mm/h or 0.1–1 mm/h, while the largest PDFs for heavy rainfall (say larger than 1 mm/h), occur with the deeper clouds (deeper than 4 km or even 12 km in some subplots). Therefore, the thinner clouds occur most likely with small rainfall, while the heavy precipitation occurs most likely with deeper clouds. The joint PDFs over the TP (Figure 7, left column) show that the change in the range of total cloud thickness associated with increasing rainfall intensity is

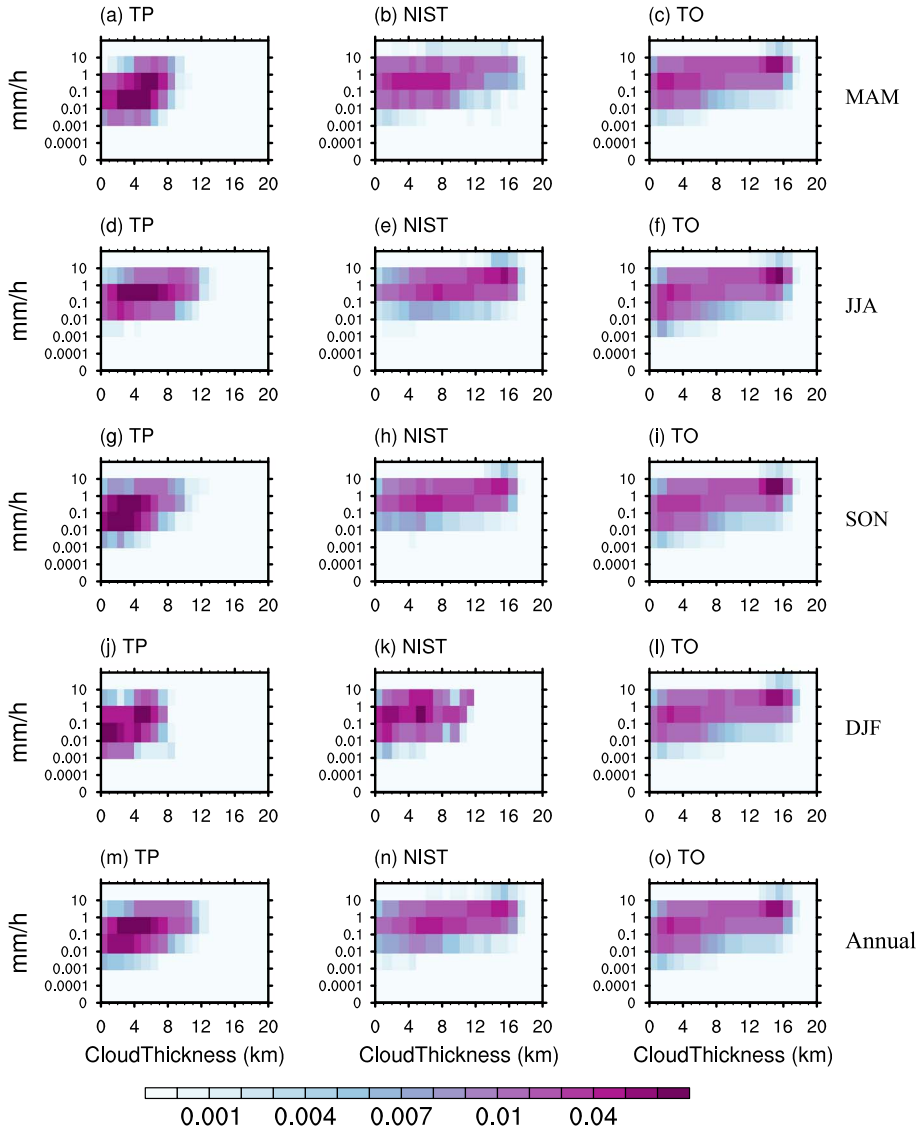

Figure 7. The joint probability distribution function (PDF) of precipitation intensity and the total cloud thickness for (a–c) spring (MAM, March-April-May), (d–f) summer (JJA, June-July-August), (g–i) autumn (SON, September-October-November), (j–l) winter (DJF, December-January-February), and (m–o) annual mean.

quite small compared to that over the NIST and TO. Even if for the heavy precipitation, the total cloud thickness rarely exceeds 12 km, while it is very common for the other two regions where the total cloud thickness may reach 17 km. The difference should be attributed to the limitation of water supply and weaker convection over the plateau terrain. Clearly, the plateau topography causes both compression effect on cloud thickness and suppression effect on the precipitation intensity.

Note that the TRMM data we used do not distinguish precipitation due to shallow convection from deep convective precipitation, but from the joint PDFs between the rainfall intensity and the total cloud thickness in Figure 7 and also the joint PDFs for the rainfall intensity and the cloud top height (Figure 8), we see that the precipitation over the TP during summer might be mainly due to shallow convection, consistent with the finding of *Fu and Liu* [2007].

3.3. The Vertical Structure of Cloud Radiative Effects (CRE)

The difference in the vertical structure of clouds in three aforementioned regions results in different cloud radiative effects (CRE). Figure 9 shows the seasonal cycles of CREs at the top of the atmosphere (TOA), in

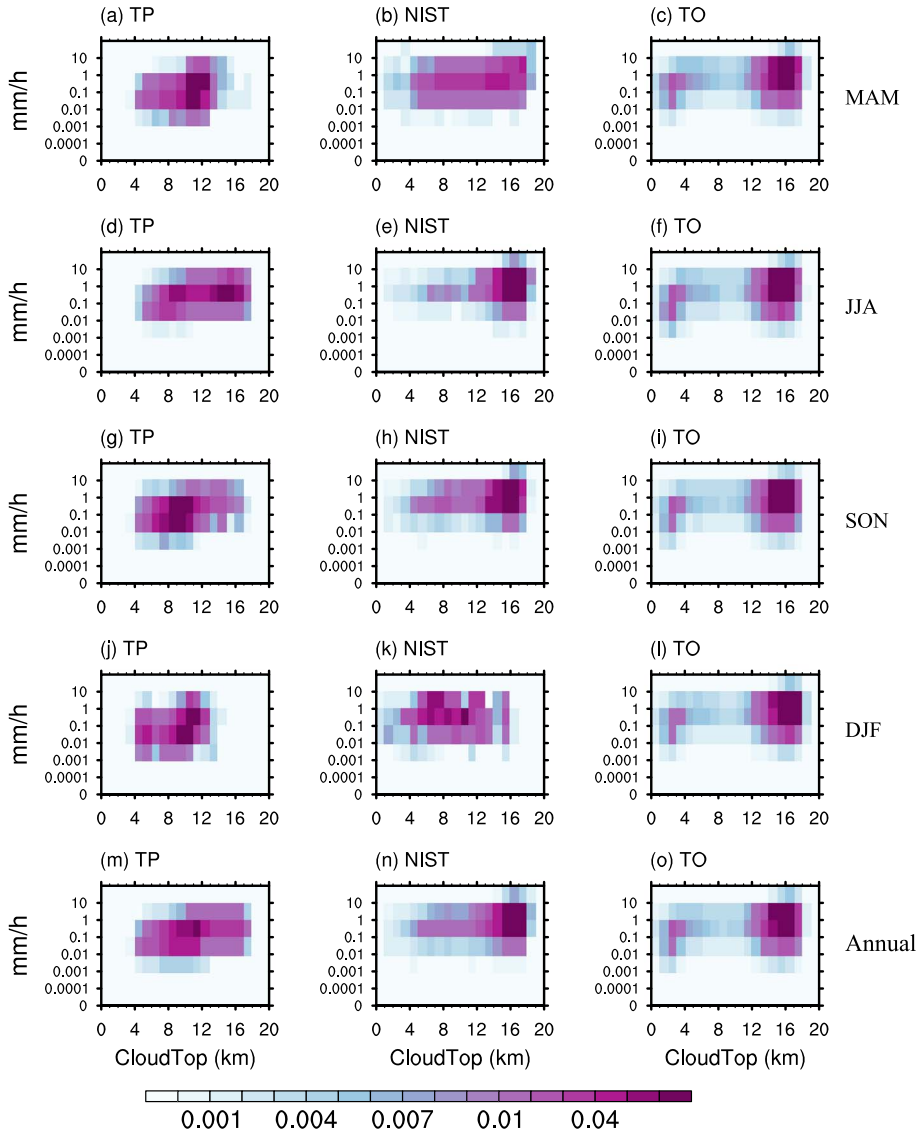

Figure 8. The joint probability distribution function (PDF) of precipitation intensity and the cloud top height for (a–c) spring (MAM), (d–f) summer (JJA), (g–i) autumn (SON), (j–l) winter (DJF), and (m–o) annual mean.

the atmosphere, and at the surface (or the bottom of the atmosphere, BOA) over the three regions. The shortwave CRE (SWCRE) is negative for both TOA and BOA due to cloud's role in reflecting solar radiation over all of the three regions. The negative SWCRE (Figure 9a) is smaller (in terms of its absolute value) at the TOA than at the BOA because of the atmospheric absorption of the reflected solar radiation by clouds, which results in net atmospheric heating. Note the atmospheric SWCRE is slightly larger over the TP than the other two regions. We will show a little later that the stronger atmospheric SWCRE over the TP is mainly related to thinner SW radiative cooling layer over low troposphere than the two other regions and also related to stronger SW heating layer over 4–8 km over the TP. The longwave CRE (LWCRE) is positive at TOA, consistent with the well-known effect of clouds in reducing outgoing longwave radiation [*Cess and Potter*, 1988]. The unique features of LWCRE over the TP include the much larger LWCRE at the BOA than the NIST and TO regions, and the net atmospheric cooling is about $-20\,W/m^2$ in contrast to the net atmospheric heating over the NIST and TO (Figure 9b).

We will see soon that these features are related to the unique vertical structure of CRE over the TP. While cautions are needed here for the difficulty in clear distinction between the surface and the atmosphere over

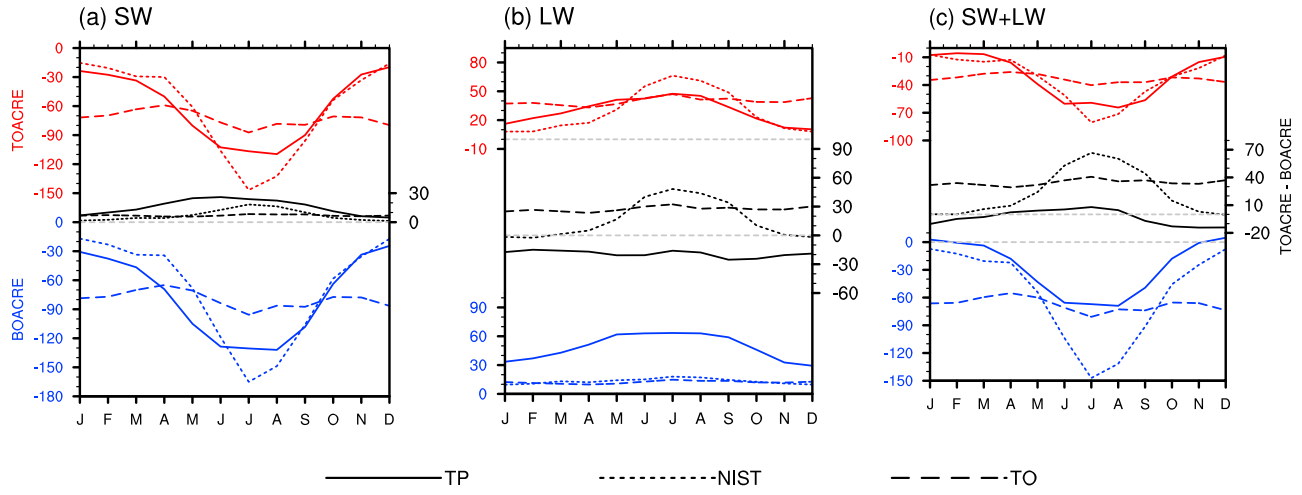

Figure 9. The seasonal cycles of (a) shortwave (SW), (b) longwave (LW), and (c) total (SW + LW) CREs at the top of the atmosphere (TOACRE), in the atmosphere (TOACRE − BOACRE), and at the bottom of the atmosphere (BOACRE). Same scale is used in the ordinates to facilitate the comparison of CREs. Unit: W m^{-2}.

the complex terrain such as TP, the independent calculation of radiative transfer supports that the above result is reliable (figures not shown).

Figure 10 shows the spatial patterns of seasonally averaged and vertically integrated atmospheric CREs. It is seen that the shortwave atmospheric heating over the TP's neighboring regions is weaker than that over the TP, especially during spring and summer (Figures 10a–10b). On the other hand, the positive longwave atmospheric heating over the TP's neighboring regions moves following the seasonal cycle of main deep

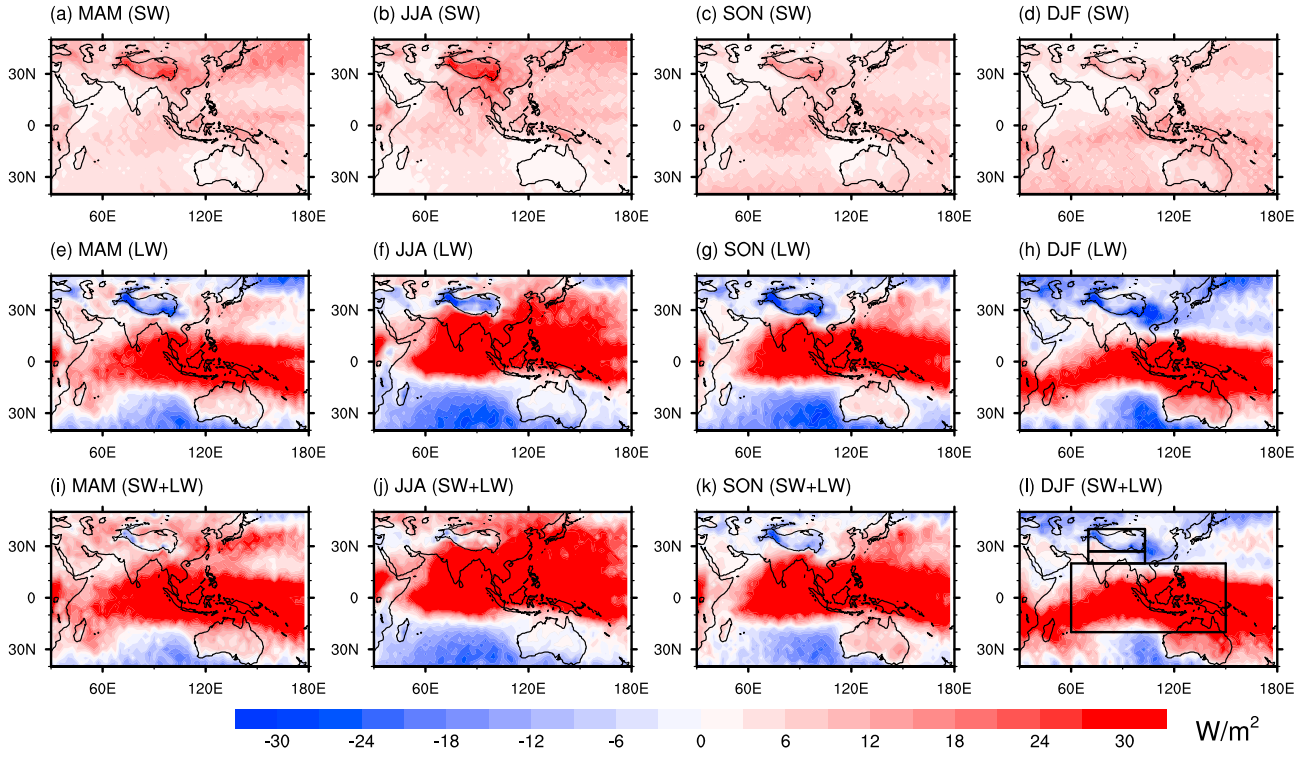

Figure 10. The spatial pattern of atmospheric cloud (a–d) shortwave (SW), (e–h) longwave (LW), and (i–l) total (SW + LW) CRE in different seasons. Black boxes in Figure 10i represent the TP, NIST, and TO regions in this study. Unit: W m^{-2}.

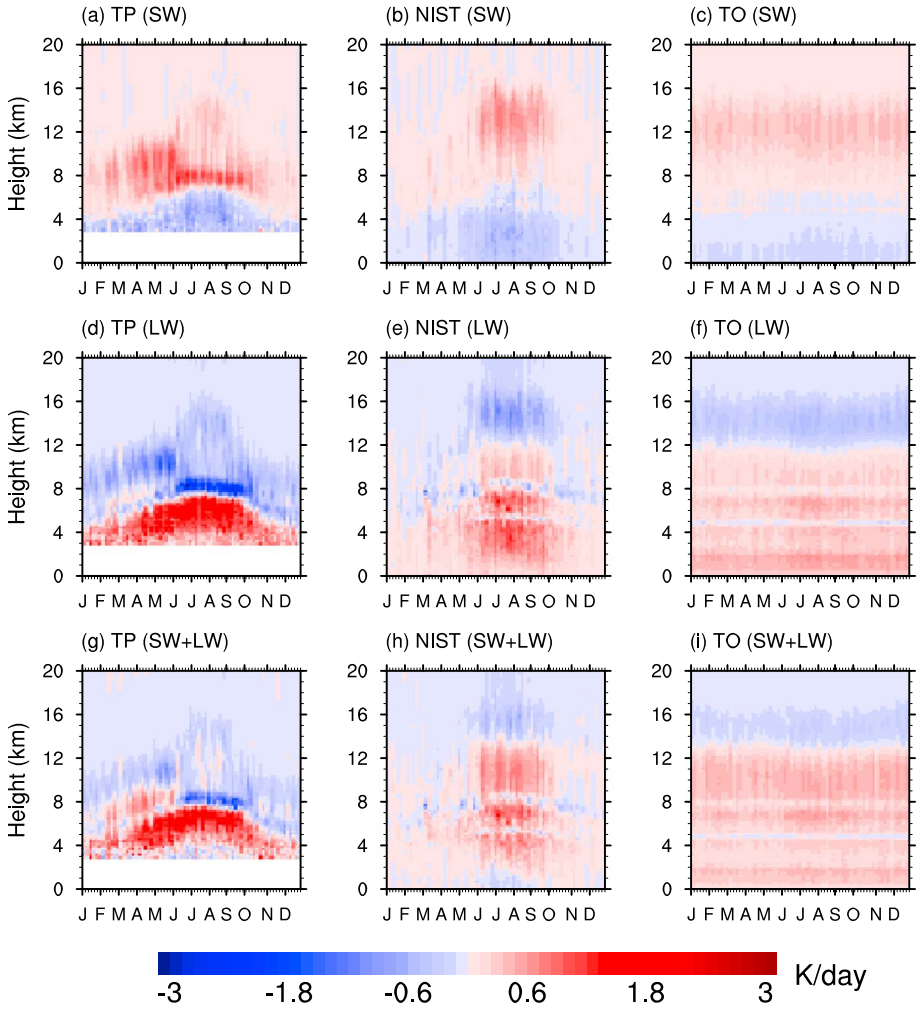

Figure 11. The seasonal cycle of the vertical profile of (a–c) shortwave (SW, top row), (d–f) longwave (LW, middle row), and (g–i) total (SW + LW, bottom row) cloud radiation effects (CRE) per unit mass over the (left column) TP, (middle column) NIST, and (right column) TO. Positive (negative) values represent heating (cooling) rate. Unit: K/d.

convection and therefore is clearly consistent with the well-known fact that longwave heating effect of clouds results from the high clouds [*Stephens and Webster*, 1981]. The compensation of longwave atmospheric cooling and shortwave heating over the TP makes the column-integrated, net atmospheric heating of clouds much weaker than its neighboring regions and closer to the condition in midlatitude to high latitude while opposed to the net atmospheric heating in tropical and subtropical regions in autumn and winter.

This does not mean that the atmospheric CRE over the TP is not important if we look further at the vertical structure of atmospheric CRE per unit mass (Figure 11, in K/d), in which the difference with other regions is more clearly shown. While it is in common over the three regions that the negative SWCRE is confined to surface and lower troposphere and there is SWCRE heating in the upper layers, and the layer with large negative SWCRE over the TP is thinner than the two other regions and has more salient seasonal cycle (Figures 11a–11c). Meanwhile, the layer with maximum SWCRE heating over the TP is much lower, mainly between 7 km and 12 km, compared to around 16 km for the NIST and TO (Figures 11a–11c). Apparently, this is consistent with the vertical distribution of clouds in Figure 3 that there are fewer high clouds over the TP, in contrast to the maximum cloud fraction of high clouds related to deep convection over the NIST and TO. Because the longwave heating effect of clouds is mainly due to the high clouds, as shown in Figures 11e and 11f for the NIST and TO, the layer with LWCRE heating is deep and nearly evenly

distributed below about 12 km. In comparison, from June to the beginning of October, the vertical structure of LWCRE over the TP is unique in that the LWCRE heating layer is shallow and confined underneath 7 km with the heating rate much larger than that in the other regions (Figure 11d). Above the shallow LWCRE heating layer is a deep LWCRE cooling layer with the maximum cooling rate located between 8 km and 12 km, just above the heating layer (Figure 11d). The vertical structure of net CRE (Figures 11g–11i) basically follows the LWCRE due to the dominance of LWCRE over SWCRE. But we note that the LWCRE cooling in the upper layer over the TP is largely canceled out by SWCRE heating, and hence, the net CRE heating or cooling above 8 km is very weak over the TP.

While the clouds over the TP have lower cloud top than other regions (Figure 8), they have stronger surface (or BOA) LWCRE than the clouds in the NIST and TO. It is well known that the LWCRE is mainly related to the high clouds and the LWCRE-caused heating acts mainly in the atmosphere, rather than at the surface, as in the cases of the NIST and TO. Over the TP, due to the uplifted topography and associated unique vertical profiles of temperature and water vapor, the net downward LWCREs otherwise heating the atmosphere become the much stronger surface LWCRE over the TP. The height of cloud top may be less important than the topography here.

The lowest panel of Figure 9b and Figure 11 suggests a larger seasonal variability in surface (or BOA) LWCRE over the TP. Except for the seasonality of cloud itself, this may also be related to larger seasonal variability over the TP in vertical structures of temperature and water vapor which are important to net LW radiation and hence LWCRE.

Radiative transfer calculations show that the unique vertical structure of CRE over the Tibetan Plateau is related to the vertical structure of liquid and solid water contents in clouds, but the detailed analysis in this regard will be presented in another paper.

4. Conclusions and Discussion

By using two data sets of CloudSat/CALIPSO and TRMM we analyze the vertical structure of clouds, its relationship with precipitation, and the CRE over the Tibetan plateau compared to its neighboring land (NIST) and ocean (TO) regions. Main conclusions are as follows:

1. The cloud amount shows seasonal variation over the TP, which presents a single peak (located in 7–11 km) during January to April and two peaks (the stronger one located in 5–8 km and the weaker one in 11–17 km separately) after mid-June, and then resumes to one peak (located in 5–10 km) after mid-August.
2. Topography-induced restriction on moisture supply leads to a compression effect on clouds, i.e., the reduction in both cloud thickness and number of cloud layers, over Tibetan Plateau. The range in the variation of cloud thickness and cloud top height corresponding to different precipitation intensity is significantly smaller over Tibetan Plateau than its neighboring regions.
3. The vertical structures of both SWCRE and LWCRE in the atmosphere over the TP show salient difference with other regions. Both the SWCRE heating and the LWCRE cooling layers in the upper atmosphere over the TP are deeper and the maximum values are located lower than that over the other regions. This is consistent with the vertical distribution of cloud amount over the TP.
4. The vertical structure of net CRE over the TP is unique compared to other regions, especially in the existence of a strong cooling layer of net CRE at the altitude of 8 km and a shallower but stronger heating layer just above the surface to 7 km from June to the beginning of October.

The unique vertical structure of CRE over the TP, especially the strong cooling layer in the altitude of 8 km in summer, may indicate unique features of the interaction between cloud, radiation, and the large-scale circulation, distinct from that in other regions such as over tropical ocean. There are still very few researches in this regard due to the lack of direct observations. The phenomena revealed in this study and ongoing observational research may promote our understanding of this important topic and the model simulation of cloud vertical structure and also the precipitation.

While the results here provide useful information on the relationship between cloud, precipitation and cloud radiative effects, our investigation is limited by the local time sampling by CloudSat/CALIPSO. More general and precise information related to the full diurnal cycle and averages need to combine with the geostationary satellites and ground-based observations.

Acknowledgments
This work is jointly funded by the National Natural Science Foundation Project (91437219 and 41275088), the Third Tibetan Plateau Scientific Experiment (GYHY201406001), and Chinese Academy of Sciences (CAS) Programme (grant XDA11010402). We are grateful for all the valuable comments from anonymous reviewers. The CloudSat/CALIPSO data were obtained from CloudSat Data Processing Center (http://cswww.cira.colostate.edu/data_dist/OrderData.php) funded by the NASA CloudSat project. The TRMM data were obtained from NASA Goddard Space Flight Center (http://pmm.nasa.gov/data-access/downloads/trmm#).

References

Cess, R. D., and G. L. Potter (1988), A methodology for understanding and intercomparing atmospheric climate feedback processes in general-circulation models, *J. Geophys. Res.*, *93*(D7), 8305–8314, doi:10.1029/JD093id07p08305.

Chen, B., and X. Liu (2005), Seasonal migration of cirrus clouds over the Asian monsoon regions and the Tibetan Plateau measured from MODIS/Terra, *Geophys. Res. Lett.*, *32*, L01804, doi:10.1029/2004GL020868.

Cooperative Institute for Research in the Atmosphere (2008), CloudSat standard data products handbook, Colorado State University, 18 pp. [Available at http://www.cloudsat.cira.colostate.edu/dataHome.php.]

Duan, A., G. Wu, and X. Liang (2008), Influence of the Tibetan Plateau on the summer climate patterns over Asia in the IAP/LASG SAMIL model, *Adv. Atmos. Sci.*, *25*(4), 518–528, doi:10.1007/s00376-008-0518-2.

Duan, A. M., and G. X. Wu (2005), Role of the Tibetan Plateau thermal forcing in the summer climate patterns over subtropical Asia, *Clim. Dyn.*, *24*(7–8), 793–807, doi:10.1007/s00382-004-0488-8.

Dufresne, J.-L., and S. Bony (2008), An assessment of the primary sources of spread of global warming estimates from coupled atmosphere-ocean models, *J. Clim.*, *21*, 5135–5144, doi:10.1175/2008JCLI2239.1.

Fu, Y., and G. Liu (2007), Possible misidentification of rain type by TRMM PR over Tibetan Plateau, *J. Appl. Meteorol. Climatol.*, *46*(5), 667–672, doi:10.1175/jam2484.1.

Gao, B. C., P. Yang, G. Guo, S. K. Park, W. J. Wiscombe, and B. Chen (2003), Measurements of water vapor and high clouds over the Tibetan Plateau with the Terra MODIS instrument, *IEEE Trans. Geosci. Remote Sens.*, *41*(4), 895–900, doi:10.1109/TGRS.2003.810704.

Hong, Y., and G. Liu (2015), The characteristics of ice cloud properties derived from CloudSat and CALIPSO measurements, *J. Clim.*, *28*, 3880–3901, doi:10.1175/JCLI-D-14-00666.1.

Huang, Y. (2013), On the longwave climate feedbacks, *J. Clim.*, *26*, 7603–7610, doi:10.1175/JCLI-D-13-00025.1.

Huffman, G. J., R. F. Adler, D. T. Bolvin, G. J. Gu, E. J. Nelkin, K. P. Bowman, Y. Hong, E. F. Stocker, and D. B. Wolff (2007), The TRMM multisatellite precipitation analysis (TMPA): Quasi-global, multiyear, combined-sensor precipitation estimates at fine scales, *J. Hydrometeorol.*, *8*(1), 38–55, doi:10.1175/jhm560.1.

Jiang, J. H., et al. (2012), Evaluation of cloud and water vapor simulations in CMIP5 climate models using NASA "A-Train" satellite observations, *J. Geophys. Res.*, *117*, D14105, doi:10.1029/2011JD017237.

Jiang, X., D. E. Waliser, J.-L. Li, and C. Woods (2011), Vertical cloud structures of the boreal summer intraseasonal variability based on CloudSat observations and ERA-Interim reanalysis, *Clim. Dyn.*, *36*(11–12), 2219–2232, doi:10.1007/s00382-010-0853-8.

Johansson, E., A. Devasthale, T. L'Ecuyer, A. M. L. Ekman, and M. Tjernström (2015), The vertical structure of cloud radiative heating over the Indian subcontinent during summer monsoon, *Atmos. Chem. Phys.*, *15*, 11,557–11,570, doi:10.5194/acp-15-11557-2015.

Jet Propulsion Laboratory (JPL) (2007), Level 2 radar-lidar GEOPROF product version 1.0 process description and interface control document, Jet Propulsion Laboratory California Institute of Technology, 20 pp. [Available at http://www.cloudsat.cira.colostate.edu/dataICDlist.php?go=list&path=/2B-GEOPROF-LIDAR.]

Jet Propulsion Laboratory (JPL) (2011), Level 2B fluxes and heating rates and 2B fluxes and heating rates w/ lidar process description and interface control document, 4 pp. [Available at http://www.cloudsat.cira.colostate.edu/data-products/level-2b/2b-flxhr-lidar?term=38.]

Kim, S.-W., E.-S. Chung, S.-C. Yoon, B.-J. Sohn, and N. Sugimoto (2011), Intercomparisons of cloud-top and cloud-base heights from ground-based Lidar, CloudSat and CALIPSO measurements, *Int. J. Remote Sens.*, *32*(4), 1179–1197, doi:10.1080/01431160903527439.

Li, Y., R. Yu, Y. Xu, and X. Zhang (2004), Spatial distribution and seasonal variation of cloud over China based on ISCCP data and surface observations, *J. Meteorol. Soc. Jpn.*, *82*(2), 761–773, doi:10.2151/jmsj.2004.761.

Li, Y., X. Liu, and B. Chen (2006), Cloud type climatology over the Tibetan Plateau: A comparison of ISCCP and MODIS/TERRA measurements with surface observations, *Geophys. Res. Lett.*, *33*, L17716, doi:10.1029/2006GL026890.

Li, Z., H. W. Barker, and L. Moreau (1995), The variable effect of clouds on atmospheric absorption of solar radiation, *Nature*, *376*(6540), 486–490.

Liu, C., E. J. Zipser, G. G. Mace, and S. Benson (2008), Implications of the differences between daytime and nighttime CloudSat observations over the tropics, *J. Geophys. Res.*, *113*, D00A04, doi:10.1029/2008JD009783.

Liu, Y., Q. Bao, A. Duan, Z. Qian, and G. Wu (2007a), Recent progress in the impact of the Tibetan Plateau on climate in China, *Adv. Atmos. Sci.*, *24*(6), 1060–1076, doi:10.1007/s00376-007-1060-3.

Liu, Y., B. Hoskins, and M. Blackburn (2007b), Impact of Tibetan orography and heating on the summer flow over Asia, *J. Met. Soc. Jpn.*, *85B*, 1–19.

Lu, C., Y. Liu, S. Niu, and S. Endo (2014), Scale dependence of entrainment-mixing mechanisms in cumulus clouds, *J. Geophys. Res. Atmos.*, *119*, 13,877–13,890, doi:10.1002/2014JD022265.

Luo, H. B., and M. Yanai (1984), The large-scale circulation and heat sources over the Tibetan plateau and surrounding areas during the early summer of 1979, Part II: Heat and moisture budgets, *Mon. Weather Rev.*, *112*(5), 966–989, doi:10.1175/1520-0493(1984)112<0966:TLSCAH>2.0.CO;2.

Luo, Y., R. Zhang, and W. Qian (2011), Intercomparison of deep convection over the Tibetan Plateau–Asian monsoon region and subtropical North America in boreal summer using CloudSat/CALIPSO Data, *J. Clim.*, *24*(8), 2164–2177, doi:10.1175/2010jcli4032.1.

Mace, J., Q. Zhang and D. P. C. Team (2012), 2B-GEOPROF-LIDAR interface control document, 13 pp. [Available at http://www.cloudsat.cira.colostate.edu/dataICDlist.php?go=list&path=/2B-GEOPROF-LIDAR.]

Naud, C. M., and Y. H. Chen (2010), Assessment of ISCCP cloudiness over the Tibetan Plateau using CloudSat-CALIPSO, *J. Geophys. Res.*, *115*, D10203, doi:10.1029/2009JD013053.

Noh, Y.-J., C. J. Seaman, T. H. Vonder Haar, D. R. Hudak, and P. Rodriguez (2011), Comparisons and analyses of aircraft and satellite observations for wintertime mixed-phase clouds, *J. Geophys. Res.*, *116*, D18207, doi:10.1029/2010JD015420.

Peng, J., H. Zhang, and Z. Li (2014), Temporal and spatial variations of global deep cloud systems based on CloudSat and CALIPSO satellite observations, *Adv. Atmos. Sci.*, *31*(3), 593–603, doi:10.1007/s00376-013-3055-6.

Ramanathan, V., R. D. Cess, E. F. Harrison, P. Minnis, B. R. Barkstrom, E. Ahmad, and D. Hartmann (1989), Cloud-radiative forcing and climate: Results from the Earth radiation budget experiment, *Science*, *243*, 57–63, doi:10.1126/SCIENCE.243.4887.57.

Reiter, E. R., and D. Y. Gao (1982), Heating of the Tibet Plateau and movements of the South Asian high during spring, *Mon. Weather Rev.*, *110*, 1694–1711, doi:10.1175/1520-0493(1982)110<1694:HOTTPA>2.0.CO;2.

Rossow, W. B., and L. C. Garder (1993), Cloud detection using satellite measurements of infrared and visible radiances for ISCCP, *J. Clim.*, *6*, 2341–2369, doi:10.1175/1520-0442(1993)006<2341:CDUSMO>2.0.CO;2.

Rossow, W. B., and A. A. Lacis (1990), Global, seasonal cloud variations from satellite radiance measurements. Part II: Cloud properties and radiative effects, *J. Clim.*, *3*, 1204–1253, doi:10.1175/1520-0442(1990)003<1204:GSCVFS>2.0.CO;2.

Rüthrich, F., B. Thies, C. Reudenbach, and J. Bendix (2013), Cloud detection and analysis on the Tibetan Plateau using Meteosat and CloudSat, *J. Geophys. Res. Atmos.*, *118*, 10,082–10,099, doi:10.1002/jgrd.50790.

Sassen, K., and Z. Wang (2008), Classifying clouds around the globe with the CloudSat radar: 1-year of results, *Geophys. Res. Lett.*, *35*, L04805, doi:10.1029/2007GL032591.

Simmons, A. J., S. M. Uppala, D. Dee, and S. Kobayashi (2006), ERA-Interim: New ECMWF reanalysis products from 1989 onwards, *ECMWF Newslett.*, *110*, 26–35.

Stephens, G. L. (2005), Cloud feedbacks in the climate system: A critical review, *J. Clim.*, *18*, 237–273, doi:10.1175/JCLI-3243.1.

Stephens, G. L., and P. J. Webster (1981), Clouds and climate: Sensitivity of simple systems, *J. Atmos. Sci.*, *38*, 235–247, doi:10.1175/1520-0469(1981)038<0235:CACSOS>2.0.CO;2.

Stephens, G. L., et al. (2002), The Cloudsat mission and the A-Train, *Bull. Am. Meteorol. Soc.*, *83*(12), 1771–1790, doi:10.1175/bams-83-12-1771.

Su, W., and J. Mao (1998), Cloud distribution characteristics over the Tibetan Plateau, *Proc. SPIE*, *3501*, 511–520, doi:10.1117/12.317724.

Wang, H., Y. Luo, and R. Zhang (2011), Analyzing seasonal variation of clouds over the Asian monsoon regions and the Plateau Tibetan region using CloudSat/CALIPSO data [in Chinese], *Chin. J. Atmos. Sci.*, *35*(6), 1117–1131.

Wang, S., Z. Han, and Z. Yao (2010a), Comparison of cloud amounts from ISCCP and CloudSat over China and its neighborhood [in Chinese], *Chin. J. Atmos. Sci.*, *34*(4), 767–779.

Wang, S.-J., W.-Y. He, H.-B. Chen, J.-C. Bian, and Z.-H. Wang (2010b), Statistics of cloud height over the Tibetan Plateau and its surrounding region derived from the CloudSat data [in Chinese], *Pleateau Meteor.*, *29*(1), 1–9.

Wielicki, B. A., R. D. Cess, M. D. King, D. A. Randall, and E. F. Harrison (1995), Mission to planet Earth: Role of clouds and radiation in climate, *Bull. Am. Meteorol. Soc.*, *76*, 2125–2153, doi:10.1175/1520-0477(1995)076<2125:MTPERO>2.0.CO;2.

Winker, D. M., W. H. Hunt, and M. J. McGill (2007), Initial performance assessment of CALIOP, *Geophys. Res. Lett.*, *34*, L19803, doi:10.1029/2007GL030135.

Wu, G. X., and Y. S. Zhang (1998), Tibetan Plateau forcing and the timing of the monsoon onset over South Asia and the South China Sea, *Mon. Weather Rev.*, *126*(4), 913–927, doi:10.1175/1520-0493(1998)126<0913:Tpfatt>2.0.Co;2.

Wu, G. X., Y. Liu, T. Wang, R. Wan, X. Liu, W. Li, Z. Wang, Q. Zhang, A. Duan, and X. Liang (2007), The influence of the mechanical and thermal forcing of the Tibetan Plateau on the Asian climate, *J. Hydrometeorol.*, *8*, 770–789, doi:10.1175/JHM609.1.

Yang, Q., Q. Fu, and Y. Hu (2010), Radiative impacts of clouds in the tropical tropopause layer, *J. Geophys. Res.*, *115*, D00H12, doi:10.1029/2009JD012393.

Yu, R., B. Wang, and T. Zhou (2004), Climate effects of the deep continental stratus clouds generated by the Tibetan Plateau, *J. Clim.*, *17*, 2702–2713, doi:10.1175/1520-0442(2004)017<2702:CEOTDC>2.0.CO;2.

Zhang, M. H., et al. (2005), Comparing clouds and their seasonal variations in 10 atmospheric general circulation models with satellite measurements, *J. Geophys. Res.*, *110*, D15S02, doi:10.1029/2004JD005021.

Zhang, Y., H. Chen, and R. Yu (2014), Vertical structures and physical properties of the cold-season stratus clouds downstream of the Tibetan Plateau: Differences between daytime and nighttime, *J. Clim.*, *27*(18), 6857–6876, doi:10.1175/jcli-d-14-00063.1.